Journal of Materials Processing Technology 232 (2016) 34–42

Contents lists available at ScienceDirect

Journal of Materials Processing Technology

journal homepage: www.elsevier.com/locate/jmatprotec

Nanosecond laser processing of $Zr_{41.2}Ti_{13.8}Cu_{12.5}Ni_{10}Be_{22.5}$ with single pulses

E. Williams, E.B. Brousseau *

Cardiff School of Engineering, Cardiff University, Cardiff CF24 3AA, UK

ARTICLE INFO

Article history:
Received 10 July 2015
Received in revised form 13 January 2016
Accepted 22 January 2016
Available online 25 January 2016

Keywords:
Nanosecond laser machining
Zr-based bulk metallic glass
Vitreloy 1
Single pulse processing

ABSTRACT

In addition to their attractive mechanical properties, the amorphous structure of bulk metallic glasses (BMGs) leads to favourable conditions for their processing using micro machining operations. At the same time, the generally high hardness and strength of such amorphous metals make short or ultra-short pulsed laser ablation a fabrication technology of interest for generating micro scale features on BMG workpieces in comparison with mechanical material removal means. In spite of this, relatively little research has been reported on the prediction and observation of the thermal phenomena that take place when processing BMGs with pulsed laser irradiation for a range of delivered fluence values and pulse lengths. Such investigations are important however as they underpin reliable laser processing operations, which in turn lead to more predicable material removal at micro scale. In this context, this paper reports complementary theoretical and experimental single pulse laser irradiation analyses conducted in the nanosecond (ns) regime for possibly the most prominent BMG material due to its relatively high glass forming ability, namely $Zr_{41.2}Ti_{13.8}Cu_{12.5}Ni_{10}Be_{22.5}$, which is also known as Vitreloy 1. To achieve this, different pulse lengths comprised between 15 ns and 140 ns and varied fluence values were considered when delivering single pulses on a Vitreloy 1 substrate using a Yb fibre laser system. A simple thermal model of the laser material interaction process for single pulses was also developed to support the observations and interpretations of the experimental data obtained. One of the main conclusions from this research, with respect to potential micro machining applications, is that shorter pulses, i.e. 25 ns and less, could lead to the formation of relatively clean craters. For higher pulse lengths, the low thermal conductivity and melt temperature of this BMG substrate mean that laser irradiation easily leads to the formation of a relatively large melt pool and thus to the re-solidification of material ejected outside craters.

1. Introduction

Metallic alloys have an internal structure that is crystalline in nature. Glass, on the other hand, does not possess a structure with the long range atomic order found in such alloys. Metallic glasses display a morphology from both of these types of materials, having metal elements and bonds, whilst possessing an amorphous internal structure. This mixture in contents for metallic glasses results in electrical and thermal characteristics, which are common to metals while it also leads to superior mechanical and chemical properties compared to their crystalline counterparts, such as an enhanced tensile strength and elastic limit as well as better corrosion resistance.

The first reported metallic glass alloy was produced at California Institute of Technology in 1960 (Klement et al., 1960) with further glassy metals formed by Chen and co-workers in the 1970's (Chen and Turnbull, 1969). The formation of bulk metallic glasses (BMGs) takes advantage of the difference in atomic sizing of all the elements present in the alloy system, which results in "confusion" upon cooling. This means that during the process used to cool down the liquid phase of the alloy, the different atoms do not organise themselves into an ordered structure in sufficient time before they become "frozen" in place. However, to avoid crystallisation when synthesising a metallic glass from its liquid state, it is essential that the cooling rate applied is higher than the critical cooling rate of the particular alloy system processed. As a result, early fabrication attempts of amorphous metals were limited to the formation of samples with thin dimensions as such specimens enabled the required fast heat dissipation rate. In the 1990's, the synthesis of metallic glasses further improved through the ability

* Corresponding author.
E-mail address: BrousseauE@cf.ac.uk (E.B. Brousseau).

http://dx.doi.org/10.1016/j.jmatprotec.2016.01.023

to bulk produce newer alloy systems in 1 mm rods (Axinte, 2012). One of the most studied BMG due to its superior glass forming ability was created in 1992 by Peker and Johnson (1993) and named Vitreloy 1, for which the composition is $Zr_{41.2}Ti_{13.8}Cu_{12.5}Ni_{10}Be_{22.5}$. This type of metallic glass exhibits a critical cooling rate of ~2 K/s (Kim et al., 1996) and has a critical casting thickness of 3 cm to 4 cm (Johnson et al., 2011).

The attractive mechanical and chemical properties of BMGs have made them candidates for a number of applications as reported by Inoue et al. (2008). These include parts for consumer goods, improved components for scientific instruments and automotive pressure sensors. Using BMGs for the production of micro-electromechanical systems (MEMS) with enhanced performances has also been an application of interest (Schroers et al., 2007). In the context of employing BMGs to develop miniaturised devices, one of the advantageous characteristics of such alloys relies on the fact that the absence of grain boundaries and crystal defects in their structure creates favourable processing conditions for generating micro and nano-scale surface features (Kumar et al., 2009). A number of material removal techniques have been investigated to structure micro and sub-micro features on as-cast BMGs including mechanical cutting (Zhu et al., 2012) and focused ion beam (Li et al., 2007), respectively. Micro machining of BMGs with high power laser systems also presents interesting fabrication opportunities due to the inherent high-throughput of such an approach and its associated ability for processing a broad range of materials regardless of their hardness. At the same time, recent developments in laser sources have resulted in significant interest for fibre lasers and their applications for micro machining. In particular, such lasers possess attractive characteristics over their Q-switched diode-pumped solid-state (DPSS) counterparts such as a relatively low cost of ownership and a flexible operating window with respect to the selection of the pulse duration, shape and repetition rate. Thus, in order to strengthen the potential of BMGs towards the cost effective development of devices with functionalities relying on features or surface structures with micro scale dimensions, it is important to conduct fundamental micro machining studies focussing on the interaction between a pulsed laser beam and such amorphous alloys.

In this context, this paper investigates the processing of a commercial BMG, Vitreloy 1, with a Yb fibre nanosecond laser system using complementary experimental and theoretical approaches. In particular, the focus of the reported research is on the single pulse processing of such a glassy alloy in order to investigate specifically the physical phenomena that are at play during the interaction between a nanosecond laser pulse with a wavelength of 1064 nm and the surface of a Vitreloy 1 sample. To achieve this, the effects of two parameters, namely the applied fluence and pulse duration, on the laser processing of Vitreloy 1 are studied through the machining of single pulse craters. The paper is organised as follows. First, in order to clarify the context of the study reported here, the next section presents a review of various investigations on the laser processing of BMGs with a number of different laser sources. Following this, the experimental and theoretical methodologies adopted in this research are described. Then, the validation of the developed single pulse model is reported. Next, the study conducted for investigating laser-material interaction using single pulses for a range of pulse durations and fluence values is presented in Section 5. Finally, conclusions are given in the last section.

2. Laser processing of bulk metallic glasses

The vast majority of the research studies that focused on the processing of BMGs with lasers can be broadly grouped into three different application domains, which are reviewed in this section, namely (1) surface treatment, (2) welding and (3) micro/nano structuring.

Surface treatment investigations are specifically concerned with the study of the laser irradiation effect on the modification of the amorphous nature of BMG materials. For example, Wu et al. (2013) studied the influence of laser processing on the microstructure and mechanical properties of three types of CuZr-based BMGs. In this case, a 180 W Nd:YAG laser with 1 ms pulse width was used and the obtained results showed that, as a consequence of the applied thermal load, crystalline precipitates could be induced in the glassy matrix of the specimens exhibiting a lower glass forming ability. For those particular samples, the compressive plasticity and the density of locally generated shear bands upon fracture was also increased compared to the corresponding amorphous, as-cast alloys. Ikutomo et al. (2008) also observed crystallisation for 2 mm thick $Zr_{55}Cu_{30}Al_{10}Ni_5$ BMG plates following irradiation with a 500 W diode laser. The presented results also showed that for a given laser power density, the reduction of the scanning speed led to more pronounced crystallisation.

For laser welding applications, the focus of the reported research studies has been on the analysis of the weld quality as well as on the formation, or otherwise, of crystalline precipitates in the re-solidified weld zone and the surrounding heat affected zone. Generally, the main motivation behind the application of laser welding for BMGs is driven by the need to broaden their application domain as the size of produced single BMG workpieces is still limited to a few centimetres in thickness. Li et al. (2006) welded $Zr_{45}Cu_{48}Al_7$ BMG plates using a laser output power of 1200 W with a spot size of 0.3 mm at different scanning speeds. The authors showed that, for a given laser irradiation setting, it was possible to generate weld joints without introducing crystallisation when operating at a sufficiently high scanning speed. A similar conclusion was reached by Kim et al. (2007) when applying microsecond pulses with a Nd:YAG laser to weld $Cu_{54}Ni_6Zr_{22}Ti_{18}$ BMG plates. Likewise, Wang et al. (2012) identified a minimum applicable scanning speed to weld 3 mm thick Ti-based ($Ti_{40}Zr_{25}Ni_3Cu_{12}Be_{20}$) BMG plates without defects or crystallisation using a 3.5 kW laser welding system. These authors also showed that when fully amorphous, the welded joint exhibited a tensile strength close to that of the base material. Chen et al. (2014) conducted laser welding tests on annealed $Zr_{55}Cu_{30}Ni_5Al_{10}$ plates using a Yb fibre laser in continuous mode. Interestingly, the study showed that the thermal annealing just above the glass transition temperature of the BMG prior to welding has a beneficial effect on the weld quality as well as on the micro hardness and bending strength of welded zones. This result was reported to be due to the fact that annealing favours nanocrystallisation while suppressing large crystal growth in the heat affected zone.

For micro and nano surface structuring, which is the application of interest in this research, existing studies have mostly been relying on femtosecond (fs) or nanosecond (ns) laser systems. For example, Sano et al. (2007) compared the ablation depths obtained between a Zr-based BMG ($Zr_{55}Al_{10}Ni_5Cu_{30}$) and its crystallised counterpart using a fs laser which delivered 100 fs pulses at 800 nm wavelength for a range of energy values comprised between 2 μJ and 900 μJ. It was found that, above 10 μJ, the ablation depth of the crystallised sample was lower than that of the BMG. This was attributed to the energy loss of hot electrons at grain boundaries that takes place during the fs laser processing of the crystallised metal. Ma et al. (2010) also used a fs laser to process the same Zr-based BMG. In this case, the specific purpose of the research was to study the formation of micrometre-spaced concentric rings on the BMG. These periodic structures were induced by the accumula-

tion of multiple defocussed pulses irradiating a fixed location on the specimen surface. The system utilised was a Ti:sapphire laser delivering 50 fs pulses at 800 nm wavelength. These authors investigated the effect of a range of laser fluence values comprised between 0.18 J/cm^2 and 5.3 J/cm^2 and a varying number of pulses on the process outcome. It was observed that, for lower laser fluence values, the concentric ring formation was driven by a non-thermal effect. In contrast, the formation of these circular features with higher fluence values appeared to be the result of a thermal process, i.e. the re-solidification of molten material. Chen et al. (2013) also used a Ti:sapphire fs laser at 800 nm wavelength on a $Pd_{40}Ni_{40}P_{20}$ BMG target. The specific focus for these authors was to demonstrate the applicability of such a laser processing approach for generating periodic nanostructures on the workpiece, which could then be used as a nano-imprinting replication master. Other reports of laser processing of BMGs but this time in the ns regime include research from Lin et al. (2012) who performed pulsed laser micro machining of Mg-based BMGs ($Mg_{65}Cu_{25}Gd_{10}$) with a 355 nm ultraviolet (UV) laser and a 1064 nm fibre laser. Both systems were operated with pulse durations of 30 ns and the fluence values considered were comprised between 6 J/cm^2 and 12 J/cm^2 for the UV laser and between 6.5 J/cm^2 and 19 J/cm^2 for the fibre laser. It was found that a higher micro machining rate was achieved using the UV laser due to the higher absorption rate of the Mg-based samples at 355 nm and the higher photon energy at such wavelength. It was also observed that the amorphous nature of the BMG samples could be retained when the lower and higher processing values were utilised for the laser power and the scan speed, respectively. Using single ns pulses, Liu et al. (2011a) reported the formation of concentric surface ripple patterns on the edge of the irradiated areas for a Vitreloy 1 sample. More specifically, the experiments were conducted with a Q-switched Nd:YAG system generating a 532 nm laser beam with 10 ns pulses and an intensity of 2.5×10^{13} W/m^2. This surface rippling phenomenon was attributed to the Kelvin–Helmholtz instability phenomenon taking place at the interface between the laser-induced plasma plume and the molten Vitreloy 1 pool. In a subsequent study, the same authors also performed single pulse ns laser ablation of Vitreloy 1 but this time in a water environment (Liu et al., 2012). The laser system used was the same as that in Liu et al. (2011a) and a fixed fluence of 238 J/cm^2 was employed. In this case, it was observed that the strong interaction between the generated plasma plume and the molten layer led to the formation of rough starfish-shaped surface structures around the ablated area. This result was reported to be due to a hydrodynamic instability phenomena referred to as the Saffman–Taylor fingering. Surface ripples formed on the edge of the laser processed area during single pulse ns laser irradiation in air were also observed by Liu et al. (2011b) when processing a different type of Zr-based BMG ($Zr_{47.7}Cu_{31}Ni_9Al_{12.3}$). In this study, the authors used a KrF excimer laser operating at a wavelength of 248 nm and with a pulse duration of 10 ns under 3.45×10^{11} W/m^2 of beam intensity.

The literature review presented above reveals that little attention has generally been paid to the study of laser processing of BMGs in the context of single pulse ablation. This is in spite of the fact that the topographical analysis of single pulse crater is beneficial for developing a better understanding of laser ablation phenomena over a range of applied process parameters. In particular, such an approach can provides important information with respect to the different thermal processes taking place during laser material interaction such as melt ejection and vaporization. In this context, the aim of this research is to study the single pulse machining of Vitreloy 1, which is arguably the most popular type of BMG, with a ns fibre laser, which possess a flexible operating window with respect to the pulse duration compared to ns Q-switched DPSS systems.

3. Methodology

3.1. Theoretical model development

Due to the fact that Vitreloy 1 is still relatively new in the field of laser processing for micro and nano structuring applications, its thermal analysis during laser machining has not been comprehensively investigated. For this reason, a simple two-dimensional theoretical model was developed to analyse the temporal and spatial evolution of the temperature in this type of substrate. This model was also used to predict the geometry of the obtained craters when subjected to an incident laser beam of varying pulse duration and delivered energy. For this theoretical study, the specific heat capacity, c_p (J/(kg K)), and the thermal conductivity, k (W/(m K)), of Vitreloy 1 were considered to be temperature dependent. However, it was assumed that its density, ρ (kg/m^3), optical absorption coefficient at 1064 nm, α (m^{-1}), and reflectivity, R, were constant. Another assumption made was that the workpiece could be represented by a semi-infinite body due to the fact that the laser spot size, the optical absorption length and the thermal penetration depth are very small compared to the workpiece dimensions. In addition, and similarly to the justification reported in Grigoropoulos et al. (1993), convection and radiation losses from the top surface of the material, on which the laser beam is incident, were neglected because of the high intensity of the laser beam utilised, which is of the order of 10^{12} W/m^2.

For laser processing in the ns regime, the absorption of the transmitted laser beam energy by electrons within the material lattice occurs at a time length which is shorter than the duration of pulses. This means that the energy absorption can be treated as being transformed directly into heat. Thus, the evolution of the temperature, T (K), in time, t (s), and in a two-dimensional space (x, z) (m), resulting from the energy absorption of a pulse into the lattice can be described using the classical Fourier heat equation:

$$\rho c_p(T)\frac{\partial T(x,z,t)}{\partial t} - \frac{\partial}{\partial z}\left(k(T)\frac{\partial T(x,z,t)}{\partial z}\right) - \frac{\partial}{\partial x}\left(k(T)\frac{\partial T(x,z,t)}{\partial x}\right) = Q(x,z,t) \quad (1)$$

where $Q(x, z, t)$ represents a volumetric heat source generated by the laser beam incident on the top surface of the BMG substrate. The variable z is the distance into the BMG target from its top surface in a direction perpendicular to the surface while x is an axis parallel to the surface of the workpiece. The heat source is formulated according to the Beer–Lambert law using the following equation:

$$Q(x,z,t) = \alpha \times (1-R) \times I(x,t) \times e^{-\alpha z} \quad (2)$$

where $I(x, t)$ describes the incident beam intensity, which is assumed to have a Gaussian profile in time and space. Using this assumption, the equation describing the spatial and temporal shape of the pulse input is as follows (Hitz et al., 2012):

$$I(x,t) = I_0 \times e^{-2\left(\frac{x}{r}\right)^2} \times e^{-4\times\ln 2\times\frac{(t-t_0)^2}{t_{pulse}^2}} \quad (3)$$

where r is the radius of the laser beam at the focal point (m), t_0 is the time at which the pulse starts (s), t_{pulse} is the full duration of the pulse at half maximum (s) and I_0 is the peak output power of the laser pulse (W/m^2), which is described with:

$$I_0 = \frac{E}{\tau\pi r^2} \quad (4)$$

where E is the pulse energy (J) and τ is the pulse duration (s). Melting of the material is taken into account in this model, which means

Table 1
Material properties utilised for Vitreloy 1.

Parameter	Value	Source
T_s (K)	937	Peker and Johnson (1993)
T_l (K)	993	Peker and Johnson (1993)
ρ (kg/m^3)	6100	Conner et al. (1997)
L_h (J/mol)	6184	Peker and Johnson (1993)
c_p (J/(kg K))	$(1/M)\times(24.9+7.5\times10^{-3}T+8.17\times10^{6}/T^2)$	Demetriou and Johnson (2004)
Molar mass M (kg/mol)	0.0603	Demetriou and Johnson (2004)
k (W/m K)	$0.0163T+0.84$	Demetriou and Johnson (2004)

that the contribution of the latent heat of fusion, L_h (J/kg), is also considered. This is achieved using the 'temperature formulation' method, which introduces a function, f_l (T), denoting the liquid volume fraction (Fachinotti et al., 1999). In this study, the liquid volume fraction is described by a ramp function, which is assumed to vary linearly between the solidus and liquidus temperatures as follows (Abderrazak et al., 2009):

$$\begin{cases} T < T_s, f_l(T) = 0 \\ T_s \le T \le T_l, f_l(T) = \dfrac{T - T_s}{T_l - T_s} \\ T > T_l, f_l(T) = 1 \end{cases} \quad (5)$$

where T_s and T_l are the solidus and liquidus temperatures, respectively. Thus, this function is added to the heat conduction equation along with the latent heat of fusion and the density to account for the latent heat contribution:

$$\rho c_p(T)\frac{\partial T(x,z,t)}{\partial t} + \rho L_h \frac{\partial f_l(T)}{\partial t} - \frac{\partial}{\partial z}\left(k(T)\frac{\partial T(x,z,t)}{\partial z}\right) - \frac{\partial}{\partial x}\left(k(T)\frac{\partial T(x,z,t)}{\partial x}\right) = Q(x,z,t) \quad (6)$$

The following initial and boundary conditions were also adopted:

- Before irradiation, the whole substrate is assumed to be at ambient temperature, i.e. $T(x, z, 0) = 300$ K.
- The bottom surface of the workpiece is kept at ambient temperature, i.e. $T(x, -\infty, t) = 300$ K.
- As mentioned earlier, the top surface is considered adiabatic, which means that:

$$k\frac{\partial T(x,z,t)}{\partial z}\Big|_{z=0} = 0 \quad (7)$$

This theoretical model was implemented in the FlexPDE software using a fixed mesh finite element discretisation. The particular material parameters used in the model are given in Table 1.

3.2. Experimental set-up

The laser system used was a 20 W pulsed Yb-doped fibre laser based on a Master Oscillator Power Amplifier (MOPA) architecture from SPI Lasers. The actual spatial profile of the intensity of the delivered laser beam was near Gaussian with an M^2 value less than 2 and the focal length was 100 mm. A precise tuning of the delivered pulses could be achieved to generate waveforms of varying durations. In this way, different pulse lengths were studied, namely 15 ns, 25 ns, 55 ns, 85 ns and 140 ns. A range of different fluence values was also considered for each of them. In order to calculate the delivered fluence, the laser spot size was estimated with the method presented by Liu (1982). In particular, this technique involves delivering a series of single pulses at varying pulse energy, E, on a sample coated with a thin film, which has a constant removal threshold. The sample used in this work was a fused silica specimen coated with a thin chromium film. Then, the measured radius, r_m, for each crater was fitted to the following equation:

$$r_m^2 = 2r_f^2 \ln\left[\frac{E}{E_{thres}}\right] \quad (8)$$

where E_{thres} is the minimum energy required for crater formation in order to extract the value of r_f, which is the radius of the laser spot. In this way, the diameter of the laser spot was calculated to be 32 μm. All laser processing experiments performed in this study were conducted in ambient air. The depth and diameter of the machined craters were measured using a White Light Interferometer (WLI) (MicroXAM from ADE Phase Shift), while their topography and the resulting material ejection were observed using a Scanning Electron Microscope (SEM) (XB1540 from Carl Zeiss). The Vitreloy 1 material was purchased as a rod 12 mm in diameter and cut into 3 mm thick disks using micro wire electro discharge machining. Prior to the laser processing operations, the BMG samples utilised were polished using a procedure tailored for hard materials and their amorphous structures confirmed with an X-ray diffraction (XRD) instrument using CuKα radiation.

4. Theoretical model validation

In order to verify that the implemented thermal model could be used reliably to complement the experimental observations obtained in this study, its validity was assessed first. To achieve this, the fluence threshold predicted by the model to induce melting for a given pulse duration was compared against that resulting from experimental data. Fig. 1 shows the theoretical temperature variations with time for various fluence values comprised between 4.9 J/cm^2 and 43.7 J/cm^2 for a pulse of 140 ns. The temperature values given in this figure are those attained at the point on the substrate located in the centre of the laser beam irradiation (i.e. with coordinates $x = 0$, $z = 0$). Based on this figure, an initial coarse observation indicates that the theoretical fluence required for reaching the melting point of $Zr_{41.2}Ti_{13.8}Cu_{12.5}Ni_{10}Be_{22.5}$ lies between 4.9 J/cm^2 and 10 J/cm^2. A more accurate estimation was derived by fitting a power law function to the plot describing the maximum temperature attained for each fluence value simulated. In this way, the theoretical fluence threshold to induce melting was estimated to be 8.0 J/cm^2. This predicted result was then compared against the experimental estimation, which was found to be 7.3 J/cm^2. In particular, this empirical fluence threshold was obtained using the method put forward by Liu (1982), which can also be used for the laser spot size calculation, as reported in the previous section. Thus, based on the fact that both the theoretical and experimental results agreed relatively well, the suitability of the implemented model was considered acceptable for the main purpose of this research, which is to study the laser material interaction process in the nano-second regime, as reported in the next section.

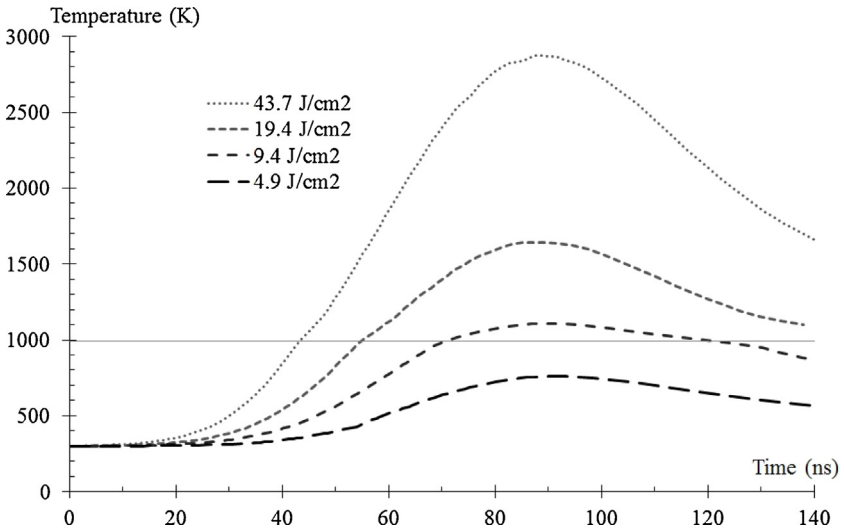

Fig. 1. Theoretical temperature evolution with time for a pulse of 140 ns with different fluence values. The horizontal line represents the melt temperature of the material, which is 993 K.

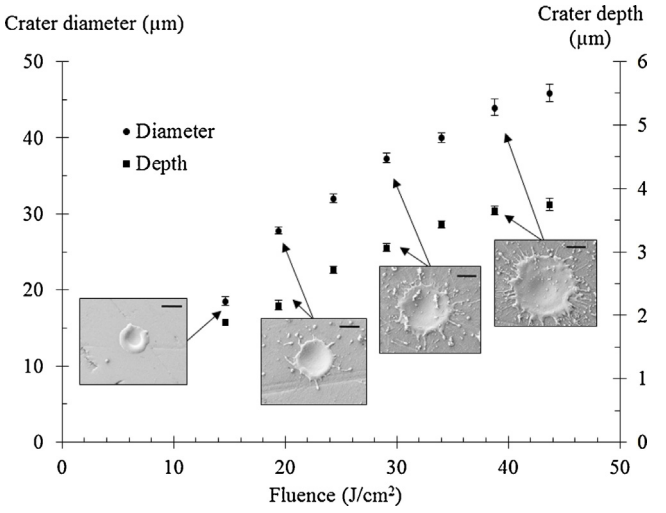

Fig. 2. Crater diameter and depth as a function of the fluence for a 140 ns pulse. Scale bars: 20 μm.

5. Single pulse experiments

5.1. Effect of the delivered fluence

Fig. 2 shows the diameter and depth of craters generated with 140 ns single pulses at varying fluence values. It can be seen from this figure that both of these process outcomes increase with the augmentation of the fluence. This conclusion was also reached for other pulse durations, i.e. 25 ns, 55 ns, and 85 ns. This is an expected observation and it results from the fact that, with the increase of the fluence for a given pulse length, the electrons within the subsystem of the material transfer a higher amount of energy to the lattice. This leads to a deeper penetration of the melt front into the workpiece and thus, to an increased amount of material that can be subjected to removal. However, it is also observed from this figure that the rate of augmentation in depth and diameter tends to reduce after about 35 J/cm^2 for this pulse length. This indicates that the mechanism of material removal gradually changes from melt ejection-dominated to vaporisation-dominated. In particular, as the latent heat of vaporisation needs to be absorbed when vaporisation occurs, this is a less efficient material removal process (Voisey et al., 2003). According to the theoretical results presented in Fig. 1 earlier for this pulse length, the maximum temperature reached for the highest fluence considered in Fig. 2 should be below 3000 K. Thus, based on the fact that the required temperature to reach explosive boiling was estimated to be about 6000 K by Jiang et al. (2015), it can be said that the vaporisation process observed here is that of normal evaporation.

Corresponding SEM micrographs of single craters for a number of fluence values are also given with Fig. 2. At the lowest fluence, 14.6 J/cm^2, it can be seen that an initial melt pool is formed and the molten material is pushed radially towards the edge of the crater. This should be mainly caused by the hydrodynamic motion of the liquid phase, which is a consequence of a gradient in the surface temperature of the material along the radial axis of the crater. More specifically, this temperature gradient is induced by the spatial distribution of the energy of the incident laser beam. As the fluence is increased over 19 J/cm^2, re-solidified material is observed outside the crater. This suggests that the recoil pressure generated by vaporisation becomes sufficiently high to overcome the surface tension of the melt pool and thus, for melt ejection to take place. Initially, this appears to happen essentially via the formation of distinct droplets and as the fluence is increased over 30 J/cm^2, the melt ejection tends to exhibit an increased occurrence of long and thin splashes. This may indicate that the melt ejection velocity increases with an augmentation in fluence, which would be consistent with observations reported for a number of other metal substrates (Voisey et al., 2003). It is also observed that at fluence values over 40 J/cm^2, two overlapping waves of melt start forming. This is attributed to the particular temporal shape of the pulse at 140 ns, which is characterised by an initial fast rise, as it takes less than 7.5 ns for an increase in signal from 10% to 90%, followed by a long trailing energy tail of about 120 ns. Thus, at fluence values over 40 J/cm^2, sufficient energy is delivered via this trailing tail for a second front of melt ejection to occur.

From the qualitative observation of the SEM micrographs, it can also be said that the volume of re-solidified melt is quite substantial. This is an indication of low thermal diffusivity (or thermal conductivity) for the irradiated substrate. In turn, this means that a relatively high thermal energy is held within a small volume upon

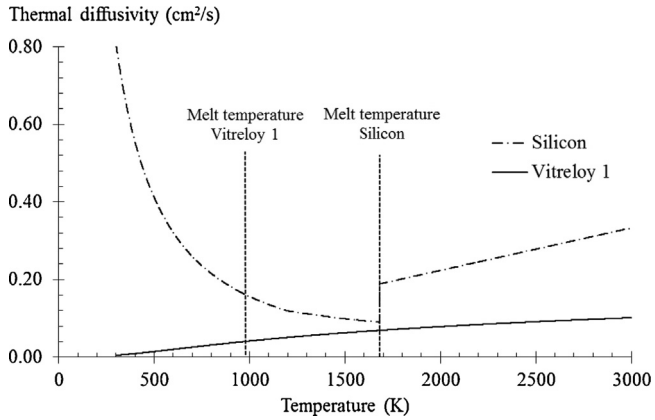

Fig. 3. Evolution of the thermal diffusivity for silicon and Vitreloy 1 ($Zr_{41.2}Ti_{13.8}Cu_{12.5}Ni_{10}Be_{22.5}$) as a function of the temperature.

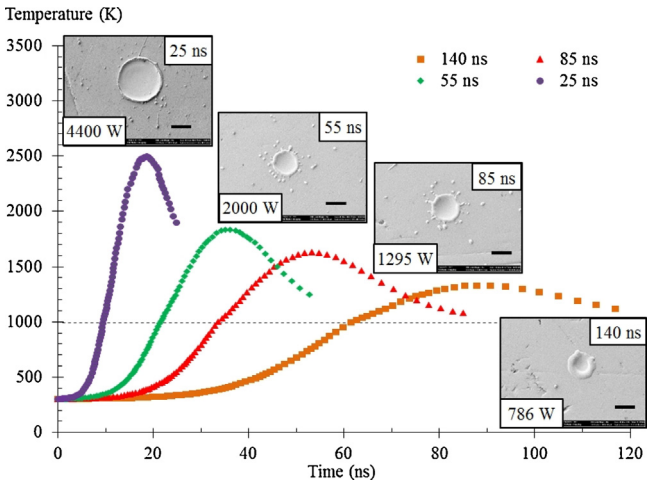

Fig. 4. Predicted temporal temperature variation at a fluence of 14 J/cm² for pulse durations of 140 ns, 85 ns, 55 ns and 25 ns. The text boxes in the bottom corner of the SEM micrographs give the peak power for each pulse duration. The horizontal line shows the melt temperature. Scale bars: 20 μm.

laser irradiation. This is consistent with the fact that single crater topographies generated on silicon by Li et al. (2014) and obtained with an identical fibre laser source and similar processing conditions did not exhibit such large melt pools. More specifically, given that the thermal diffusivity of silicon is higher than that of $Zr_{41.2}Ti_{13.8}Cu_{12.5}Ni_{10}Be_{22.5}$ across both their solid and liquid states (see Fig. 3), Vitreloy 1 is comparatively more likely to be affected by the re-solidification and deposition of material expelled from the melt pool during laser processing. The thermal diffusivity, D, plotted in Fig. 3 was calculated using equation (9) below:

$$D = \frac{k}{\rho c_p} \tag{9}$$

The temperature-dependent values for the density, specific heat capacity and thermal conductivity of silicon were computed from Yoo et al. (2000). The values used for these thermal properties in the case of Vitreloy 1 were those reported earlier in Table 1.

When considering the non-crystalline nature of the BMG used in this study, it is also worth mentioning that, when ablating an amorphous Ni-based specimen and its equivalent crystalline alloy using single pulses with a μs laser system, Quintana et al. (2009) reported the formation of a larger melt pool for the amorphous sample compared with the crystalline substrate. In addition, Yamasaki et al. (2004) found that, in the case of Vitreloy 1, its amorphous and supercooled liquid state exhibit a smaller thermal conductivity than its crystalline counterpart. A similar observation was made between a number of glasses and other crystalline substances by Kittel (1949), who attributed this effect to the disordered atomic structure of amorphous materials, which restricts the mean free path of phonons and thus, limits the thermal conductivity. Thus, the formation of relatively large melt pools for Vitreloy 1, as observed in Fig. 2, is attributed to the coupling that occurs between the inherently low melt temperature of Vitreloy 1 and its comparatively small thermal conductivity (or thermal diffusivity), which favours confined volumetric heating.

5.2. Effect of the peak power

Fig. 4 shows the theoretical temperature evolution obtained with a fixed fluence of 14 J/cm² for different pulse durations, namely 25 ns, 55 ns, 85 ns and 140 ns. The typical crater topography and the peak power value achieved for each of these pulse lengths is also given in this figure.

The model predicts that the melt temperature of the substrate is reached for each single pulse processing condition considered here, which is confirmed by the corresponding SEM micrographs shown in Fig. 4. The crater obtained for the 140 ns pulse corresponds to that already commented upon in the previous section. In particular, a melt pool with a relatively thick circular edge is formed in this case. As the peak power is increased, via the reduction in pulse length, melt ejection takes place. This is particularly visible for craters formed with the pulse lengths of 85 ns and 55 ns, which correspond to peak power values of 1295 W and 2000 W, respectively. This is indicative of the existence of vapour pressure over the melt pool. At the highest peak power, 4400 W, which is obtained with a pulse of 25 ns, the delivered fluence enables the onset of melting but melt expulsion is reduced substantially in this case. This could caused by the combined effect of (1) the pulse duration being too short to allow enough time for the pressure over the molten layer to increase sufficiently and (2) the crater having a thinner melt pool at reduced pulse length due to the associated reduced thermal penetration depth. Qualitatively, it is also observed that the diameter of the craters becomes larger with the reduction of the pulse length. This is attributed to the fact that, with the corresponding increase in peak power, the surface area of the substrate that reaches a temperature value above the melting point within the irradiated spot also increases.

A single pulse trial was also conducted using a shorter pulse length of 15 ns. However, the delivered fluence could not be set-up as high as 14 J/cm² in this case. It was 7.6 J/cm² instead. This corresponds to a pulse peak power of 4070 W. The crater topography obtained in this way is reported with Fig. 5. It is interesting to note that, for this experiment, surface deformations are present immediately outside the edge of the crater to a value of about 2.5 μm in a radial direction. This area may be referred to as the heat affected zone (HAZ) given that it is influenced by the heat distribution from the laser beam but has not reached the melt temperature. This is confirmed with the theoretical data shown in Fig. 6 where a small region outside the edge of the crater, with a similar width to that observed with the SEM micrograph of Fig. 5 is subjected to heating above the glass transition temperature of the material, T_g, which is equal to 623 K (Waniuk et al., 2001). This suggests that the material exhibited a viscous behaviour in this region and was deformed plastically. As reported in Section 2 earlier, Liu et al. (2011a) also observed similar surface rippling effects when machining Vitreloy 1 with an Nd:YAG solid state laser with 10 ns pulses, a wavelength of 532 nm and an intensity of 2.5×10^{13} W/m². For comparison, the intensity used in the result presented in Fig. 5 was an order of magnitude lower; more precisely 5.1×10^{12} W/m². These authors concluded that the created patterns were not due to light inter-

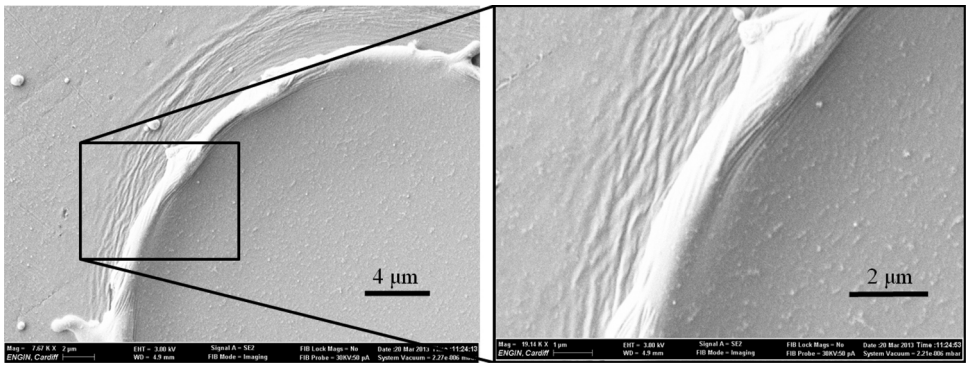

Fig. 5. SEM micrographs of a crater machined at 15 ns with a fluence of 7.6 J/cm^2.

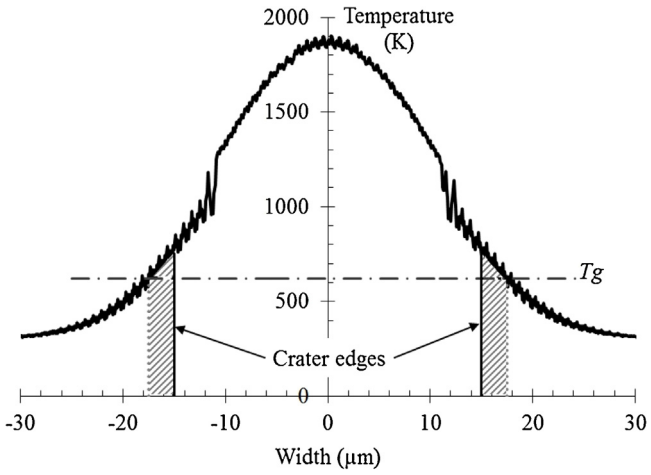

Fig. 6. Spatial temperature distribution on the top surface of Vitreloy 1 for a pulse of 15 ns with a fluence of 7.6 J/cm^2. The vertical solid lines represent the edge of the crater, which has a diameter of about 30 μm. The hatched area shows the region heated above T_g while located outside the crater.

ference given that the spacing of the ripples was larger than the wavelength of the beam. Instead, they attributed the ripples to the Kelvin-Helmholtz instability arising from the differences in densities and velocities of the molten material and the plasma plume generated in the centre of the laser ablated region. Due to the lower intensity used here compared to that of Liu et al. (2011a) and, consequently, the lower temperatures experienced, it is unlikely that plasma was formed at all. This suggests that the ripples are caused by a different effect. Lin et al. (2012) also reported ripples outside grooves micro-machined on an Mg-based BMG using pulsed nanosecond lasers at 355 nm and 1064 nm. They attributed the formation of these wrinkles to the heat accumulation in the HAZ, causing heating above the glass transition temperature and leading to the softening of the material. Based on the spatial temperature profile presented in Fig. 6, it is likely that the ripples formed in Vitreloy 1 with the particular laser parameters used in this study are a consequence of the combined effect of (1) the material in the HAZ being above T_g, (2) the raised crater edge being relatively thin, thus leaving the surface of the HAZ exposed, and (3) the radial force exerted on the HAZ by the vapour pressure. It is worth mentioning however, that further investigations are required to elucidate in a comprehensive manner the causes of this phenomenon as a function of the irradiance of the incident laser beam.

5.3. Varying pulse length and fluence value

To complete this study, Fig. 7 shows the full set of data measured for the depths and diameters of single craters generated at the different pulse durations of 25 ns, 55 ns, 85 ns and 140 ns for various fluence values. The results displayed in this figure show that both of these craters dimensions increase with the augmentation of the fluence for all the pulse lengths investigated. This was already observed and discussed in Section 5.1 above in the case of the 140 ns pulse. The reported data generally indicate that for a given fluence value, the depth of the craters increases with the augmentation of the pulse duration. This is a consequence of the laser beam being incident on the material for longer at higher pulse lengths and thus, allowing more time for the heat to penetrate within the material and its temperature to increase above the melting point. In particular, the thermal penetration depth, l_t, is expressed as:

$$l_t \approx 2\sqrt{D\tau} \tag{10}$$

where D is the diffusivity and τ is the pulse duration. Therefore, a reduced thermal penetration, and thus a smaller ablation depth, is associated with shorter pulses. Besides, it can be observed in Fig. 4, in the case of different pulse lengths for a fixed fluence value that the time during which the temperature of the material stays above

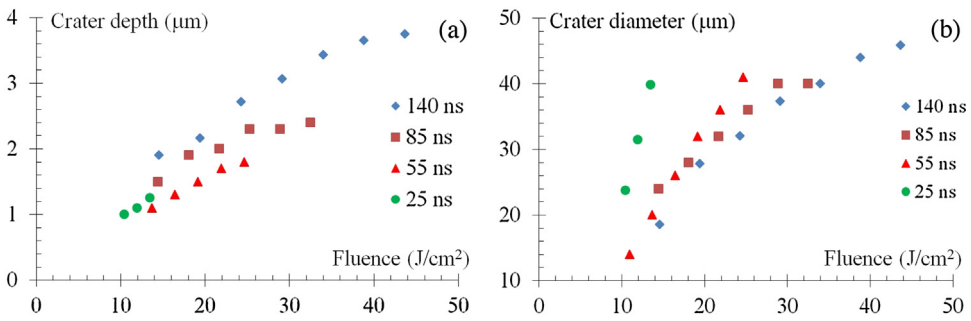

Fig. 7. Measured crater (a) depths and (b) diameters for different pulse durations and fluence values.

its melting point increases with the pulse duration. This allows more time for the melt front to propagate through the material. Combined with fact that longer pulses have an extra tail of energy, removal of material from craters is aided by sustaining further vaporisation and ejection of material via recoil pressure. The diameter of the generated craters tends to increase as the pulse length reduces for a fixed fluence value. This observation becomes particularly more pronounced as the value of the fluence considered is increased. This is attributed to the peak power effect as mentioned in the previous section.

Finally, an X-ray diffractometry (XRD) analysis using CuKα radiation was also conducted when processing the material with a fluence of 70 J/cm^2. It is worth noting that this analysis did not show evidence of crystalline precipitates being introduced in the amorphous material. Thus, given that the fluence value used for this XRD test was higher than the range of values considered in the reported study, it is expected that the processing conditions utilised in this research for single pulse irradiation did not lead to crystallisation of the Vitreloy 1 material. This is consistent with observations already reported for single pulse processing of Zr-based BMG substrates in the ns regime such as that by Liu et al. (2012) and Liu et al. (2011b). In particular, it is expected that the heating and cooling rates experienced in this case are too fast for crystalline phases to be formed.

6. Conclusions

This paper presented complementary theoretical and experimental single pulse laser irradiation results conducted in the nanosecond regime for the BMG $Zr_{41.2}Ti_{13.8}Cu_{12.5}Ni_{10}Be_{22.5}$, which is also known as Vitreloy 1. To achieve this, different pulse lengths comprised between 15 ns and 140 ns and with varied fluence values were considered when delivering single pulses using a Yb fibre laser. This study benefited from the flexibility of such a laser system with respect to the delivered pulse length in order to reduce the uncertainty associated with studying processing outcomes for various pulse durations via the alternative utilisation of different laser set-ups. The resulting crater topographies were discussed based on the possible occurrence of different thermal phenomena such as hydrodynamic motion of the melt pool at low fluence values and melt ejection induced by the recoil pressure at higher fluence. In summary, the most important conclusions that can be stated from this research are as follows:

- Nanosecond laser processing of $Zr_{41.2}Ti_{13.8}Cu_{12.5}Ni_{10}Be_{22.5}$ with fibre lasers is potentially a suitable solution for the large area micro machining of such BMG. However, as it is often the case with metal substrates, re-solidification and deposition of material expelled from the generated craters can be detrimental to the achieved machined quality at such small scale. This is attributed to the coupling that occurs between the inherently low melt temperature of this amorphous material and its comparatively small thermal conductivity, which favours confined volumetric heating.
- The formation of relatively clean and shallow craters could be achieved using a pulse length of 25 ns, and shorter, for peak power values reaching around 4000 W. In this case however, surface ripples may be visible just outside the edge of the craters. For the particular processing conditions used in this study, this was attributed to the combined effect of (1) the BMG material in the heat affected zone being above the glass transition temperature and (2) the radial force induced by the vapour pressure while (3) the reduced thickness of the crater edge means that the ripples surface are not covered by re-solidified melt

Acknowledgements

The reported research was funded by the Engineering and Physical Sciences Research Council (ESPRC) and the Interreg IVB NWE programme through the EcoLaserFact project. The authors also gratefully acknowledge the financial support provided by SPI Lasers. All data created during this research are openly available from Cardiff University data archive at http://dx.doi.org/10.17035/d.2016.0008119129. Finally, the authors would also like to acknowledge the help of Dr Christopher Von Ruhland with the SEM work at the Central Biotechnology Services at Cardiff University.

References

Abderrazak, K., Kriaa, W., Ben Salem, W., Mhiri, H., Lepalec, G., Autric, M., 2009. Numerical and experimental studies of molten pool formation during an interaction of a pulse laser (Nd:YAG) with a magnesium alloy. Opt. Laser Technol. 41, 470–480.

Axinte, E., 2012. Metallic glasses from 'alchemy' to pure science: present and future of design, processing and applications of glassy metals. Mater. Des. 35, 518–556.

Chen, H.S., Turnbull, D., 1969. Formation, stability and structure of palladium–silicon based alloy glasses. Acta Metall. 17 (8), 1021–1031.

Chen, Y.C., Chu, J.P., Jang, J.S.C., Hsieh, C.W., Yang, Y., Li, C.L., Chen, Y.M., Jeng, J.Y., 2013. Replication of nano/micro-scale features using bulk metallic glass mold prepared by femtosecond laser and imprint processes. J. Micromech. Microeng. 23 (3), 035030.

Chen, B., Shi, T.L., Li, M., Yang, F., Yan, F., Liao, G.L., 2014. Laser welding of annealed $Zr_{55}Cu_{30}Ni_5Al_{10}$ bulk metallic glass. Intermetallics 46, 111–117.

Conner, R.D., Rosakis, A.J., Johnson, W.L., Owen, D.M., 1997. Fracture toughness determination for a beryllium-bearing bulk metallic glass. Scr. Mater. 37 (9), 1373–1378.

Demetriou, M.D., Johnson, W.L., 2004. Modeling the transient flow of undercooled glass-forming liquids. J. Appl. Phys. 95 (5), 2857–2865.

Fachinotti, V.D., Cardona, A., Huespe, A.E., 1999. A fast convergent and accurate temperature model for phase-change heat conduction. Int. J. Numerical Methods Eng. 44, 1863–1884.

Grigoropoulos, C.P., Park, H.K., Xu, X., 1993. Modeling of pulsed laser irradiation of thin silicon layers. Int. J. Heat Mass Transfer 36 (4), 919–924.

Hitz, C.B., Ewing, J.J., Hetch, J., 2012. Introduction to Laser Technology. Wiley, Hoboken, New Jersey.

Ikutomo, R., Tsujikawa, M., Hino, M., Kimura, H., Yubuta, K., Inoue, A., 2008. Crystallisation by laser for Zr based bulk metallic glasses. Int. J. Cast Metals Res. 21 (1–4), 148–151.

Inoue, A., Wang, X.M., Zhang, W., 2008. Developments and applications of bulk metallic glasses. Rev. Adv. Mater. Sci. 18 (1), 1–9.

Jiang, M.Q., Wei, Y.P., Wilde, G., Dai, L.H., 2015. Explosive boiling of a metallic glass superheated by nanosecond pulse laser ablation. Appl. Phys. Lett. 106, 021904 (5 pages).

Johnson, W.L., Kaltenboeck, G., Demetriou, M.D., Schramm, J.P., Liu, X., Samwer, K., Kim, C.P., Hofmann, D.C., 2011. Beating crystallization in glass-forming metals by millisecond heating and processing. Science 332, 828–833.

Kim, Y.J., Busch, R., Johnson, W.L., Rulison, A.J., Rhim, W.K., 1996. Experimental determination of a time–temperature-transformation diagram of the undercooled $Zr_{41.2}Ti_{13.8}Cu_{12.5}Ni_{10.0}Be_{22.5}$ alloy using the containerless electrostatic levitation processing technique. Appl. Phys. Lett. 68, 1057–1059.

Kim, J.H., Lee, C., Lee, D.M., Sun, J.H., Shin, S.Y., Bae, J.C., 2007. Pulsed Nd:YAG laser welding of $Cu_{54}Ni_6Zr_{22}Ti_{18}$ bulk metallic glass. Mater. Sci. Eng. A 449–451, 872–875.

Kittel, C., 1949. Interpretation of the thermal conductivity of glasses. Phys. Rev. 75 (6), 972–974.

Klement, W., Willens, R.H., Duwez, P., 1960. Non-crystalline structure in solidified gold–silicon alloys. Nature 187, 869–870.

Kumar, G., Tang, H.X., Schroers, J., 2009. Nanomoulding with amorphous metals. Nature 457, 868–872.

Li, B., Li, Z.Y., Xiong, J.G., Xing, L., Wang, D., Li, Y., 2006. Laser welding of $Zr_{45}Cu_{48}Al_7$ bulk glassy alloy. J. Alloys Compd. 413 (1–2), 118–121.

Li, K., Sparkes, M., O'Neill, W., 2014. Comparison between single shot micromachining of silicon with nanosecond pulse shaped IR fiber laser and DPSS UV laser. IEEE J. Selected Top. Quantum Electron. 20 (5), 0900807.

Lin, H.K., Lee, C.J., Hu, T.T., Li, C.H., Huang, J.C., 2012. Pulsed laser micromachining of Mg–Cu–Gd bulk metallic glass. Opt. Lasers Eng. 50 (6), 883–886.

Liu, Y., Jiang, M.Q., Yang, G.W., Guan, Y.J., Dai, L.H., 2011a. Surface rippling on bulk metallic glass under nanosecond pulse laser ablation. Appl. Phys. Lett. 99 (19), 191902.

Liu, W.D., Ye, L.M., Liu, K.X., 2011b. Micro-nano scale ripples on metallic glass induced by laser pulse. J. Appl. Phys. 109 (4), 043109.

Liu, Y., Jiang, M.Q., Yang, G.W., Chen, J.H., Guan, Y.J., Dai, L.H., 2012. Saffman–Taylor fingering in nanosecond pulse laser ablating bulk metallic glass in water. Intermetallics 31, 325–329.

Liu, J.M., 1982. Simple technique for measurements of pulsed Gaussian-beam spot sizes. Opt. Lett. 7 (5), 196–198.

Ma, F.X., Yang, J.J., Zhu, X.N., Liang, C.Y., Wang, H.S., 2010. Femto second laser-induced concentric ring microstructures on Zr-based metallic glass. Appl. Surf. Sci. 256, 3653–3660.
Peker, A., Johnson, W.L., 1993. A highly processable metallic glass: $Zr_{41.2}Ti_{13.8}Cu_{12.5}Ni_{10.0}Be_{22.5}$. Appl. Phys. Lett., 2342 (3 pages).
Quintana, I., Dobrev, T., Aranzabe, A., Lalev, G., Dimov, S., 2009. Investigation of amorphous and crystalline Ni Alloys response to machining with micro-second and pico-second lasers. Appl. Surf. Sci. 255, 6641–6646.
Sano, T., Takahashi, K., Hirose, A., Kobayashi, K., 2007. Femtosecond laser ablation of $Zr_{55}Al_{10}Ni_5Cu_{30}$ bulk metallic glass. Mater. Sci. Forum 539–543, 1951–1954.
Schroers, J., Pham, Q., Desai, A., 2007. Thermoplastic forming of bulk metallic glass—a technology for MEMS and microstructure fabrication. J. Microelectromech. Syst. 16 (2), 240–247.
Voisey, K.T., Kudesia, S.S., Rodden, W.S.O., Hand, D.P., Jones, J.D.C., Clyne, J.W., 2003. Melt ejection during laser drilling of metals. Mater. Sci. Eng. A 356, 414–424.
Wang, G., Huang, Y.J., Shagiev, M., Chen, J., 2012. Laser welding of $Ti_{40}Zr_{25}Ni_3Cu_{12}Be_{20}$ bulk metallic glass. Mater. Sci. Eng. A 541, 33–37.
Waniuk, T.A., Schroers, J., Johnson, W.L., 2001. Critical cooling rate and thermal stability of Zr–Ti–Cu–Ni–Be alloys. Appl. Phys. Lett. 78 (9), 1213–1215.
Wu, G.J., Li, R., Liu, Z.Q., Chen, B.Q., Zhang, T., 2013. Effects of the laser surface treatment on the mechanical properties of CuZr-based bulk metallic glasses. Sci. China Phys. Mech. Astronomy 56 (5), 925–927.
Yamasaki, M., Kagao, S., Kawamura, Y., Yoshimura, K., 2004. Thermal diffusivity and conductivity of supercooled liquid in Zr_{41} Ti_{14} Cu_{12} Ni_{10} Be_{23} metallic glass. Appl. Phys. Lett. 84 (23), 4653–4655.
Yoo, J.H., Jeong, S.H., Greif, R., Russo, R.E., 2000. Explosive change in crater properties during high power nanosecond laser ablation of silicon. J. Appl. Phys. 88 (3), 1638–1649.
Zhu, Z., Zhou, X., Liu, Q., Lin, J., Zhao, S., 2012. Fabrication of micro-structured surfaces on bulk metallic glasses based on fast tool servo assisted diamond turning. Sci. Adv. Mater. 4, 906–911.